NSG 7129

EQUATIONS OF STATE AND IMPACT-INDUCED SHOCK-WAVE ATTENUATION ON THE MOON*

Thomas J. Ahrens
Seismological Laboratory
California Institute of Technology
Pasadena, California 91125

and John D. O'Keefe
Department of Earth and Space Sciences
University of California
Los Angeles, California 90024

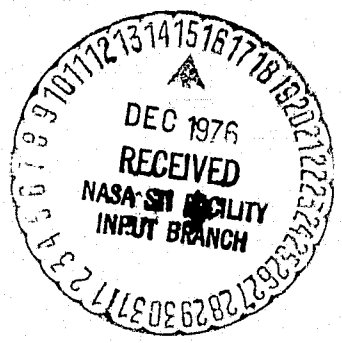

*Contribution Number 2844 , Division of Geological and Planetary Sciences; California Institute of Technology; Pasadena, California 91125

Abstract

Current equation-of-state formulations, used for finite-difference cratering flow calculations, are cast into a framework permitting comparison of peak pressures attained upon impact of a sphere, with a half-space, along the impact symmetry axis, to one-dimensional impedance match solutions. On the basis of this formulation and application of thermochemical data, the regimes of melting and vaporization are examined. For the purpose of identifying material which will, upon isentropic release from the impact-induced shock state, result in a solid just brought to its melting point, i.e., incipiently melted (IM); completely melted (CM); just brought to its boiling point, i.e., incipiently vaporized (IV); and completely vaporized (CV) state, the pressures at which the critical isentropes intersect the Hugoniots of iron and gabbroic anorthosite (GA) are examined in detail. The latter rock type is assumed to be representative of the lunar highlands. The Hugoniot pressures, for which IM, CM, IV, and CV will occur upon isentropic expansion, are calculated to be 2.2, 2.6, 4.2, and 16.8 Mbar, respectively. For the high pressure phase (hpp) assemblage of GA, modelled as a mixture of plagioclase in the hollandite structure and pyroxene in the perovskite structure, IM, CM, IV, and CV are calculated to occur upon isentropic expansion from Hugoniot states at 0.43, 0.52, 1.02, and 5.9 Mbars, respectively. The spatial attenuation of shock pressure along the impact axis is found to be clearly represented by two regimes, if the peak pressure, P, and radius normalized to that of the projectile, r, are fitted to expressions of the form $P \propto r^a$. At distances from 1.3 to 2.1 projectile radii into a GA target, the constant, a, is on the order of -0.2. This low-attenuation rate, near-field regime, extends further into the target at the slower impact velocities and arises because of the slightly divergent flow associated with the penetration of a spherical projectile. For the near-field impact regime, an impact at

5 km/sec of an iron object with a GA surface will induce CM for GA but the iron will remain solid. At 15 km/sec, partial vaporization (PV) occurs for both GA and iron, whereas at 45 km/sec, CV occurs in both materials. In the case of a GA meteoroid striking a GA surface at 5 km/sec, partial melting results at 5 km/sec, PV occurs at 15 km/sec, and CV occurs in the near-field at 45 km/sec. At greater radii, in the far-field regime, the exponent, a, varies systematically from -1.45 to -2.15 for impacts of GA onto GA as the impact velocity is increased from 5 to 45 km/sec. For an iron projectile, the exponent, a, varies from -1.67 to -2.95 as the impactor velocity increases from 5 to 45 km/sec. By comparison, the equivalent value of a, reported for both contained and surface explosions in various rocks is $\sim$ -2. It is suggested that, given field data on shock attenuation (based on identification of various shock metamorphic features versus distance), overall crater size, and some chemical data as to the type of meteoroid which produced a crater, quantitative bounds on the impact velocity of the meteorite may be obtained.

Introduction

The formulation of an equation-of-state for a rock type which we believe is typical of the lunar highland province, gabbroic anorthosite (GA), provides an opportunity to investigate two important and related problems regarding impact phenomena. These are:

1) The impact velocities, and hence shock pressures, required to bring the meteorite and target material to the melting point, i.e., incipient melting (IM), induce complete melting (CM), and produce a liquid at the boiling point, i.e., incipient vaporization (IV), and completely vaporize (CV) upon isentropic release is examined. We consider a highland terrane cratered by meteorites having equations-of-state ranging from iron to GA.

2) The spatial attenuation of peak shock-pressures in a GA composition, again, as the result of impact of objects having equations-of-state similar to iron and GA.

It has been only recently determined that, even in very large and ancient astroblemes, geochemical evidence (via analyses of the minor siderophile element contents of impact melts and ejecta (Morgan et al., 1975; Lambert, 1976)) allows specification of the causative meteorite. Moreover, recent quantitative studies of the effect of shock on minerals and their application to the spatial distribution of shock metamorphic features within in-situ shocked rock, can be used to infer distinct bounds on the spatial shock attenuation rate (Robertsen and Grieve, 1977). If in addition the spatial attenuation rate can be related to the meteorite size and velocity, then improved estimates can be obtained of the chemistry, mass, and velocity of the meteoroids which have bombarded the earth's zone as a function of time (Dence, 1972). Much of the required data is not now available for lunar craters. However, if the moon formed and evolved near the earth, the late cratering history of the earth should, with minor modification, be applicable to the moon.

In the present paper we obtain, within the framework of a two-phase Tillotson equation-of-state model the impedance-match solutions specifying the peak pressure upon impact of a GA lunar surface by meteoroids of GA and iron in the 5 to 45 km/sec range (O'Keefe and Ahrens, 1975, 1976). We then apply the available thermochemical data for the low pressure phase (lpp) assemblage and a theoretical model for the high pressure phase (hpp) assemblage to construct critical release adiabats which define regimes in the pressure (P) - volume (V) plane which specify IM, CM, IV, and CV. Finally we fit the results of a series of hypervelocity impact, finite-difference, flow calculations specifying the spatial on-axis peak pressure attenuation due to the shock wave and compare these to previous calculations and measurements of pressure attenuation from explosions.

Conditions for One-Dimensional Impact

It is useful for the purposes of (a) providing an analytic comparison with finite-difference impact calculation and (b) obtaining an estimate of the impact velocity required to induce melting and vaporization in the target and impactor, to obtain one-dimensional impedance match solutions for an assumed equation-of-state. As in our previous treatments of impact flows produced upon the impact of a meteorite with a planetary surface (O'Keefe and Ahrens, 1975, 1976), we employ a P-V-E (specific internal energy), dependent equation-of-state of the form first proposed by Tillotson (1962). In the compressed region this is given by

$$P = \left[a + \frac{b}{\left(\frac{E}{E_o \eta^2} + 1 \right)} \right] \frac{E}{V} + A\mu + B\mu^2 \qquad (1)$$

where a = 0.5 is the polytropic constant minus 1, at high temperature. The constant, b, is defined such (a + b) is the STP Grüneisen parameter, $\gamma \equiv V \left(\frac{\partial P}{\partial E} \right)_V$, and A is the bulk modulus. Here $\eta = V_o/V$ and $\mu = \eta - 1$, where V_o is the STP specific volume. The parameters b, B, and E_o are obtained by fitting to Thomas-Fermi calculations of the equation-of-state in the 10^2 Mbar range, and Hugoniot data. The parameters for GA (Table 1) are based on previous shock wave measurements on lunar sample 15418 (Ahrens et al., 1973). As in O'Keefe and Ahrens (1976), we consider the equilibrium equation-of-state for GA to have discreetly different Tillotson parameters which specify the lpp and hpp assemblage. For the latter, hpp, assemblage, stable above ∿150 kbar, we assume plagioclase has the density corresponding to the hollandite structure and pyroxene has a density corresponding to the perovskite structure. The effect of applying this relatively complex,

but realistic equation-of-state to the description of the impacts onto GA is examined in some detail by O'Keefe and Ahrens (1976).

For convenience we define, E = 0, for the lpp at STP. To invert Equation 1 to the P-u_s (particle velocity) plane, the energy term for a Hugoniot state in the hpp regime is given by

$$E = P(V_{oo} - V)/2 - E_{TR} \qquad (2)$$

where V_{oo} is the lpp, specific volume and E_{TR} is the increase in internal energy in going from the lpp to the hpp assemblage at STP.

It should be noted that if the E_{TR} term is not included in Equation 2, the resultant Hugoniot curve generated would be that of the metastable Hugoniot (McQueen et al., 1967). Moreover we note that in applying the definition of η and μ for describing the hpp, the initial specific volume used, V_o, is that of the hpp. In calculating the Hugoniot curve for GA (lpp) and for iron, $V_{oo} = V_o$ and $E_{TR} = 0$. Upon eliminating E between Equations 1 and 2, the Hugoniot pressure, $P = P_H$, is given analytically upon solution of the following quadratic equation where V (and hence μ and also η) is the independent variable

$$a'P_H^2 + b'P_H + c' = 0 \qquad (3)$$

Here

$$a' = \frac{s}{k}\left[\frac{as-1}{V}\right] \qquad (4a)$$

$$b' = (a + b)s/V - 1 + E + R(1-2as/V)/k + \ell s/k \qquad (4b)$$

$$c' = E_{TR}^2\, a/(kV) - E_{TR}(a + b)/V + \ell(1-E_{TR}/k) \qquad (4c)$$

where

$$s = (V_{oo} - V)/2 \tag{4e}$$

$$k = E_o \eta^2 \tag{4f}$$

$$\ell = \mu A + \mu^2 B \tag{4g}$$

The negative sign is used in the usual quadratic formula. Once $P_H(V)$ along the Hugoniot, centered at V_{oo}, is calculated, the corresponding value of u_p is simply calculated from the Rankine-Hugoniot equation

$$u_p = [P_H(V_{oo} - V)]^{1/2} \tag{5}$$

By solving Equation 3 at a series of specific volumes, the P_H-u_p relations given in Figure 1 are obtained from the parameters in Table 1. Straightforward application of the method of impedance matching (Duvall and Fowles, 1963)(matching pressure and particle velocity), and application of the Rankine-Hugoniot equations yield the peak shock states defined in Tables 2 and 3 for impact of iron and GA projectiles on a GA half-space.

To calculate the amount of melting and vaporization that occurs in an impact event, the release isentropes for IM, CM, IV, and CV were calculated using the Tillotson equation-of-state (Equation 1). The calculation of the isentropes requires that at least one state along the desired isentrope be known initially. These initial states are typically the internal energy or temperature at one atmosphere pressure. To obtain the internal energy contents, at one atmosphere pressure of iron required for IM (1809°K), CM, IV, (3145°K), and CV, we have utilized enthalpy and entropy data tabulated in the JANAF Tables (1965). In the case of GA, the above melting and vaporization processes are incongruent, and an approximate treatment was used for simplicity. Following the rock modelling scheme of Ahrens and O'Keefe (1972), GA was assumed to comprise a mixture of 0.714 (mass fraction) anorthite, and 0.286, enstatite. Using the JANAF thermochemical data,

through the $MgSiO_3$ melting point (1798°K) and into the liquid, and extrapolating using the entropy systematics described in Ahrens and O'Keefe (1972), the energy and entropy for incipient and complete vaporization is inferred. Assumptions regarding volitilzation are made on the basis of oxide volatility and are discussed by Ahrens and O'Keefe (1972). In the case of $CaAl_2Si_2O_8$, a similar but even less certain extrapolation was employed using the thermochemical data tabulated in Robie and Waldbaum (1968) and, again, the systematics of Ahrens and O'Keefe. The densities, at one atmosphere, given in Table 1 for IM, CM, and IV for the lpp and hpp assemblages of GA and iron are obtained from Equation 1.

Only in the case of iron can meaningful comparisons be made with other theoretical treatments and the actual densities at CM and IV. Table 1 gives densities of 7.36 and 6.10 g/cm^3 for CM and IV, respectively. Interpolating, the results of the Mie-Grüneisen reduction of the iron data by McQueen et al. (1970) to 1809° yields a considerably lower density, 6.696 g/cm^3, for CM. The CRC Handbook (1970) lists density values ranging from 6.99 to 7.24 g/cm^3 for iron at the liquidus, slightly lower, but in good agreement with those calculated from Equation 1. For IV, at 3145°K, the CRC Handbook gives density values ranging from 5.84 to 5.93 g/cm^3 which again is close to, but still slightly lower than, the 6.10 g/cm^3 value indicated in Table 1.

The onset of IM, CM, IV, and CV upon expansion (assumed isentropic) from Hugoniot states even for the one-dimensional case is of interest. We have calculated the P-V isentropes which pass through the states IM, CM, and IV specified in Table 1 at atmospheric pressure and high temperatures using Equation 1 and found their intersection with the Hugoniot curves (Table 4). In the case of iron and the lpp of GA, this is a straightforward procedure which merely involves numerically calculating the locus of V, P, and E_s (energy) states reached by an isentropic process which satisfies the energy integral along the isentrope

$$E_s = -\int_{V(IM,CM,orIV)}^{V} V(P,E)\, dP \qquad (6)$$

In principle, the actual value of the entropy along one of the isentropes, so calculated, is not explicitly specified but, in fact, requires an additional assumption equivalent to a thermodynamic model for C_P or C_v, the specific heat at constant pressure or volume. Instead, for the lpp we have used the available thermodynamic data for enstatite and anorthite, to separately estimate the entropy associated with the critical isentropes for IM, CM, and IV using the method outlined in Ahrens and O'Keefe (1972). (These data are utilized in calculating the critical isentropes for the hpp assemblage below.)

In the case of CV, the pressure is obtained by using the distended formulation of the Tillotson equation-of-state:

$$P = \frac{aE}{V} + \left\{ \frac{bE/V}{\frac{E}{E_o\eta^2}+1} + A\mu e^{-\beta[(V/V_o-1)-1]} \right\} e^{-\alpha[(V/V_o-1]^2} \qquad (7)$$

in the regime where

$$1 > V/V_o \qquad \text{for } E > E_{CV}$$

where $\alpha = \beta = 5$, and E_{CV} is the CV energy at standard pressure. In the partial vaporization regime

$$V_o > V \text{ and } E_{IV} < E < E_{CV}$$

where E_{IV} is the energy associated with IV. We utilize the interpolation relation (Allen, 1967; Hageman and Walsh, 1970)

$$P = \frac{(E - E_{IV})\, P_E + (E_{CV} - E)\, P_C}{(E_{CV} - E_{IV})} \qquad (8)$$

where P_E refers to the pressure calculated from Equation 7, the distended region, and P_C refers to the pressure calculated from Equation 1, the compressed region.

The straightforward calculation of the isentrope (Equation 6) using the distended formulation Tillotson equation-of-state and starting at a one atmosphere pressure state at complete vaporization leads to unreasonable pressures ($\simeq 10^2$ Mbar) for the intersection of the complete vaporization isentrope with the Hugoniot. The reason for this is that the second term in Equation 7 does not have the correct form in the distended regime, where μ is negative. The correct cohesive energy, $\simeq E_{CV}$, is not obtained by taking $\left| \int_{V=V_{IV}}^{V=\infty} P\,dV \right|$. This problem was partially circumvented by choosing a reference state for complete vaporization, which did not involve the distended region of the equation-of-state. To this end, we adopted the approach of Zeldovich and Raizer (1967), who demonstrate, for single phase materials, that the isentrope that passes through the vapor-liquid critical point has a specific internal energy equal to approximately twice the binding energy at standard volume. Because of this assumption the curves shown in Figures 2 through 4 for CV should be considered approximate.

The construction of release isentropes for the hpp assemblage (Figure 4) which is used as a model for GA, requires two independent assumptions in addition to the parameters of the P, V, E equation-of-state:

1) The entropy difference between the lpp and hpp assemblage; no data presently exists giving the slope of pertinent phase boundaries.

2) A model for the specific heat for the assemblage.

Although more elaborate methods have recently been suggested for estimating entropies of phases based on detailed knowledge of crystal structure (e.g., Saxena, 1976), we have used the method of Fyfe (1958) to obtain the entropy of the hpp

assemblage. This method sums the entropies of the equivalent oxide mixture (data obtained from Robie and Waldbaum, 1968). By using the STP entropy of stishovite, this procedure probably provides a good approximation, as the major effect of the assumed phase changes in both pyroxene and plagioclase is the increase of Si^{+4} coordination from four to six O^{-2} ions. Upon mass weighting entropies for the plagioclase and pyroxene hpp mixture, the transition entropy at STP is given by:

$$\text{lpp} \rightarrow \text{hpp} \quad ; \quad \Delta S^{298°K}_{TR,P=0} = -0.188 \times 10^7 \text{ ergs/gm°K} \qquad (9)$$

Recognizing the shortcomings of the Debye theory for describing C_V, when applied to silicates (Kieffer and Kamb, in preparation), we have assumed an equivalent STP, Debye temperature, Θ_D, for the hpp assemblage. Using the density-Debye temperature relation proposed for oxides by Anderson (1965), a value of $\Theta_D = 1029°K$ is obtained. The entropy, at high temperature at atmospheric pressure for the hpp assemblage, is then calculated from

$$S^T_{hpp} = S^{298°K}_{hpp} + \int_{298°K}^{T} (C_p/T)\, dT \qquad (10)$$

where, taking into account the entropy of the known lpp assemblage, and Equation 9, $S^{298°K}_{hpp} = 0.534 \times 10^7$ ergs/gm°K.

From the thermodynamic relations:

$$C_P = C_V\left(\frac{\Theta_D}{T}\right) \Big/ \left[1 - C_V\left(\frac{\Theta_D}{T}\right)\left(\frac{\partial V}{\partial E}\right)_P \frac{\gamma}{V} T\right] \qquad (11)$$

and from Equation 1, it follows that

$$\left(\frac{\partial V}{\partial E}\right)_P = \left\{\frac{a}{V} + \frac{b}{V\chi} - \frac{bE}{V\chi^2}\left[\frac{1}{E_o}\left(\frac{V}{V_o}\right)^2\right]\right\}\left\{\frac{aE}{V^2} + \frac{bE}{\chi V^2} + \frac{2bE^2}{\chi^2 V_o^2 E_o} + \frac{AV_o}{V^2} + 2B\left(\frac{V_o}{V} - 1\right)\frac{V_o}{V^2}\right\}^{-1} \tag{12}$$

and

$$\gamma = a + \frac{b}{\chi} - \frac{bE}{\chi^2}\left[\frac{1}{E_o}\left(\frac{V}{V_o}\right)^2 + 1\right] \tag{13}$$

where $\chi = E/E_o$

The variation of Θ_D with volume follows from

$$(\partial\Theta_D/\partial T)_P = -\gamma\alpha \tag{14}$$

where

$$\alpha = \frac{C_V}{V}\left(\frac{\partial V}{\partial E}\right)_P\left[1 + \frac{1}{V}\left(\frac{\partial V}{\partial E}\right)_P \gamma T\right] \tag{15}$$

In order to obtain the internal energies, relative to the lpp at STP, for the hpp at one atmosphere, such that the entropy value associated with the critical isentropes for IM, CM, IV, and CV are the same as for the lpp, we have simultaneously solved Equations 10-15, using T, the absolute temperature as the independent variable. Thus upon isentropic release from a shock state either in the lpp or hpp regime to one atmosphere and high temperature, and achieving

states corresponding to IM, CM, IV, or CV, the entropy of the material is the same, however, the isentropi paths from high pressure differ for the lpp and hpp cases, inferring that reverse transformation from the hpp occurs.

We have not yet compared the results of the Debye theory, when used with the Tillotson formulation as described in Equations 12-15, when the high temperature entropy has been explicity measured.

To describe the low cohesion of iron or GA, we have assumed $P_C = 0$, when $V_o/V < 0.99$ and $V_o/V < 0.995$ respectively. This corresponds to a dynamic tensile strength of 0.64 and 0.71 kbar, respectively. The latter physical quantities are both poorly constrained experimentally, although recent measurements of the tensile strength of novaculite and quartzites (Shockley et al., 1973) report some data in this range. By assuming $P_C = 0$ upon tensile failure, a physical model of the formation of a fragment dust and coexisting vapor is implicitly assumed. The total pressure upon failure results from only the gaseous (P_E) component of a mixture of dust and gas. Using Equations 1, 6, and 7, and the assumption concerning dynamic brittle failure to dust, the release isentropes shown in Figures 2, 3, and 4 are calculated.

Results

Applying the above detailed formulation of the equation-of-state of GA, the impact flow nd energy partitioning resulting from the interaction of a series of hypothetical iron and GA meteorites with a GA planetary surface (half-space) are calculated for impact velocities ranging from 5 to 45 km/sec. Previous results for energy partitioning and ejecta distributions upon impact of a 10 cm diameter, 15 km/sec iron object are given in O'Keefe and Ahrens (1976). Ejecta (0.5 cm, initial zone size) distributions and energy partitioning versus impact velocity will be presented elsewhere (O'Keefe and Ahrens, in preparation). Because the shape of the isentropes for the hpp

assemblage of GA strongly controls peak pressure decay, c.f., O'Keefe and Ahrens (1976), and field data relating to spatial shock attenuation are beginning to become available, c.f., this volume (Robertsen and Grieve, 1977), initial calculations of shock attenuation along the impact, symmetry axis are presented in Figures 5 and 6 and Table 5. The scatter is largely the result of the rezoning procedure in the calculation. As previous workers have noted (e.g., Gault and Heitowit, 1963; Bjork and Rosenblatt, 1965; Heyda and Riney, 1965), two regimes of attenuation are to be expected. These are indicated as near- and far-field in Table 5. Within the precision of the present calculations, centerline peak pressure decay in the near- and far-field is described in terms of:

$$\log_{10}(P - Mbar) = a \log_{10}(R/R_o) + b \qquad (15)$$

where P is the centerline pressure, R is the distance from the point of impact and R_o the initial meteoroid radius. In the near-field regime, the peak pressure may be obtained from the one-dimensional impedance match solution (Tables 3 and 4). The agreement with impedance match solutions indicated in Figures 5 and 6 appears to be closer, the higher the impact speed, as $R \rightarrow 0$. This may be due to shorter time steps in the calculation at the higher impact speeds. The slow spatial decay rate observed in the near-field is insensitive to both impact velocity and impactor type. In the present case of a spherical projectile, the near-field shock attenuation undoubtedly results from the slightly divergent flow induced in the target as the projectile imbeds itself into the target. In the case of the normal impact of a flat-nosed cylinder or rod, or in the assumed constant-hemisphere energy model of Gault and Heitowit, no attenuation, i.e., a = 0, is expected in the near-field regime. The onset of the characteristic far-field attenuation rate begins at depths corresponding to $\sim$1.6 to $\sim$2.1 projectile radii for the case of iron impacting GA as the impact velocity decreases from 45 to 5 km/sec. In the case of GA impacting GA, the far-field rates are established

at depths of from ∿1.3 to ∿1.6 projectile radii, as the impact velocity decreases from 45 to 5 km/sec. Dienes and Walsh (1970) have shown as part of their late-stage equivalence studies of hypervelocity impact that late-stage far-field flows are insensitive to the exact shape of the impactor, provided the axial to radial dimensions of the impactor are roughly comparable.

Comparison of the present results with other attenuation calculations and measurements are of interest. Dienes and Walsh found good agreement between their computer solution with experimental data, over a range of ∿10 to 1000 kbar, for the impact at 7.3 km/sec of an aluminum sphere with an aluminum half-space. The centerline particle velocity in this case, which is to first-order proportional to shock pressure, decays as, $a \simeq -2$, which is comparable to the value of "a", listed in Table 5, for the far-field, in this impact velocity range. A larger set of experimental impact data, up to ∿8 km/sec, for various aluminum projectiles is shown to satisfy a relation comparable to present results, where $a \simeq -1.6$ (Billingsley, 1969). Gault and Heitowit (1963), on the basis of their constant energy, hemisphere model, calculate, for the impact at 6.35 km/sec of an aluminum sphere onto basalt, (similar to the present An → An calculation) an initial pressure decay rate with $a \simeq -3$ to -4, which is considerably greater than predicted here. However, at the point where the shock has decayed to pressures on the order of $\sim 10^2$ kbar, their indicated attenuation rate is considerably slower than is predicted here.

Since the cratering effects of large explosions are often used for scaling of impact flows to greater dimensions than those available from results of experiments, it is of interest to compare pressure decay rates from near-surface and contained explosions. A large number of such data are summarized by Cooper (1973), who finds a decay coefficient of the centerline pressure of a $\simeq -2$ is compatible with field data for both contained and surface explosions.

This is close to the value found, for example, for An → An at 15 km/sec. Also, Butkovich and Borg (1974) demonstrated that the decay of the experimentally observed shock pressure in the range 650 to ∿1 kbar surrounding the 5 kton, Hardhat nuclear explosion in granodiorite also gave a a $\simeq$ -2 dependence. Moreover, they point out that in general, calculational results such as presented here, always give, to a first approximation, the decay rates in terms of pre-flow, i.e., Eulerian coordinates, whereas attenuation inferred from post-flow shock metamorphic features, must for meaningful comparisons, be corrected such that material motion, after the shock wave has passed, is taken into account.

Discussion

The major new result described here, is that different impact velocities, and meteorite shock impedances give rise to significantly different spatial peak shock attenuation rates in the far-field.

We anticipate that present calculational results will prove useful in placing bounds on the shock pressures, experienced by both in-situ rocks and ejecta, in the vicinity of impact craters, which petrologic and geochemical analyses indicate are partially melted, melted, or, incongruently vaporized. Moreover, (a) given the size of a crater, and hence a measure of the total projectile energy, (b) some knowledge of the chemistry, and hence shock impedance, of the impactor and (c) a measure of the spatial rate of peak shock-pressure attenuation (probably inferred from shock metamorphic features) we believe it will be possible, on the basis of the present results to estimate the impact velocity associated with a given crater. Although the required knowledge of crater size, meteoroid impedance, and spatial shock decay rate is now limited to only a few terrestrial craters, we hope the methodology presented will be useful in inferring impact velocities and cratering histories for other terrestrial planets.

Acknowledgements

This research supported under NASA Grant, NSG 7129. We appreciate the computational assistance of M. Lainhart, José Helu, and J. Huber and the opportunity to present this material at the Symposium to a critical audience. We have profited from critical comments on this manuscript offered by Raymond Jeanloz.

References

Ahrens, T. J., and O'Keefe, J. D.: 1972, The Moon, 4, 214-249.

Ahrens, T. J., O'Keefe, J. D., and Gibbons, R. V.: 1973, (Suppl. 4) Geochimica et Cosmochimica Acta. 3, 2575-2590.

Allen, R. T.: 1967, General Dynamics, General Atomic Division, Special Nuclear Effects Laboratory Report, GAMD-7834A, p. 25.

Anderson, O. L.: 1965, Physical Accoustics3B, ed. by W. P. Mason, Academic Press, 43-95.

Billingsley, J. P.: 1969, Proc. AIAA Hypervelocity Impact Conference, Paper #69-361, Vol. III, AIAA, p. 10.

Bjork, R. L. and Rosenblatt, M.: 1965, Proc. Seventh Hypervelocity Impact Symposium, IV, Martin Marietta Corp., Tampa, Florida, Vol. 4, pp. 195-211.

Butkovich, T. R. and Borg, I. Y.: 1974, Lawrence Livermore Laboratory Report UCRL-75594, p. 31.

Chemical Rubber Handbook of Chemistry and Physics,: 1970, 50th Ed., B 225-226.

Cooper, H. F., Jr.: 1973, R & D Associates, Santa Monica, Ca., Rpt. DNA 3245F, p. 85.

Dence, M. R.: 1972, Proc. 24 Int. Geol. Cong., Sect. 15, 77-89.

Dienes, J. K. and Walsh, J. M.: 1970, High Velocity Impact Phenomena, ed. by R. Kinslow, Academic Press, 46-104.

Duvall, G. E. and Fowles, G. R.: 1963, High Pressure Physics and Chemistry 2, Ed. by R. S. Bradley, Academic Press, 209-292.

Fyfe, W. S. and Verhoogen, J.: 1958, Metamorphic Reactions and Metamorphic Facies, ed. by W. S. Fyfe, F. J. Turner and J. Verhoogen, Mem. 73, Geol. Soc. Am., 21-51.

Gault, D. E., and Heitowit, E. D.: 1963, Proc. Sixth Hypervelocity Impact Symposium, Cleveland, Ohio, Vol. 2, pp. 419-456, (unpublished).

Hageman, L. J., and Walsh, J. M.: 1970, Systems, Science, and Software Report, 3SR-350, Vol. 1, p. 139

Heyda, T. F. and Riney, T. D.: 1965, Proc. Seventh Hypervelocity Impact Symposium, IV, Martin Marietta Corp., Tampa, Florida, Vol. 3, pp. 75-122.

JANAF Thermochemical Tables: 1976, Thermal Research Laboratory, Dow Chemical Company, Midland, Mich., Clearinghouse for Federal Scientific and Technical Information, PB 168-370.

Lambert, P.: 1977, The Moon, this volume.

McQueen, R. G., Marsh, S. P., and Fritz, J. N.: 1967, J. Geophys. Res. 72, 4999-5036.

McQueen, R. G., Marsh, S. P., Taylor, J. W., Fritz, J. N., and Carter, W. J.: 1970, in R. Kinslow (ed.), High-Velocity Impact Phenomena, pp. 294-416, Academic Press.

Morgan, J. W., Higuchi, H., Ganapathy, R., and Anders, E.: 1975, Proc. Lunar Sci. Conf. (6th), 1609-1623.

O'Keefe, J. D., and Ahrens, R. J.: 1975, Proc. Sixth Lunar Sci. Conf., 2831-2844.

O'Keefe, J. D. and Ahrens, T. J.: 1976, Proc. Seventh Lunar Sci. Conf., (in press).

Robertson, P. B. and Grieve, R. A. F.: 1977, The Moon, this volume.

Robie, R. A. and Waldbaum, D. R.: 1968, Geol. Survey Bull. 1259, p. 265.

Saxena, S. K.: 1976, Science 143, 1241-1242.

Shockley, D. A., Petersen, C. F., Curran, D. F., and Rosenberg, J. T.: 1972, Stanford Research Institute Report, PYU-1087, pp. 70.

Tillotson, J. H.: 1962, General Atomic Report GA 3216, p. 137.

Zeldovich, Y. B. and Raizer, Y. P.: 1966, Physics of Shock Waves and High Temperature Phenomena, Academic Press, New York, Vol. II.

TABLE I

Complete Equation of State Parameters

Material	Normal Density (gm/cm^3)	b	A (Mbar)	B (Mbar)	Eo (10^{12}ergs/gm)	Incipient Melting			Complete Melting			Incipient Vaporization			Complete Vaporization	
						Energy[b] (10^{12}ergs/gm)	Density[a] (gm/cm^3)	Entropy[c] (10^7ergs/gm°K)	Energy[b] (10^{12}ergs/gm)	Density[a] (gm/cm^3)	Entropy[c] (10^7ergs/gm°K)	Energy[b] (10^{12}ergs/gm)	Density[a] (gm/cm^3)	Entropy[c] (10^7erg/cm°K)	Energy[b] (10^{12}ergs/gm)	Entropy[c] (10^7ergs/gm)
Iron	7.80	1.5	1.279	1.05	0.095	0.0105	7.43	d	0.0132	7.36	d	0.024	6.10	d	0.0867	d
Gabbroic Anorthosite (lpp)	2.936	0.145	0.705	0.751	4.89	0.0176	2.80	2.663	0.02065	2.77	2.837	0.0472	2.57	3.517	0.1816	7.10
Gabbroic Anorthosite (spp)	3.965	0.128	2.357	1.258	18.0	0.00575[b]	3.89	2.663	0.00964	3.88	2.837	0.0319	3.79	3.517	0.16836	7.10

a) At 1 atmosphere and high temperature.

b) With respect to gabbroic anorthosite, lpp at STP.

c) With respect to gabbroic anorthosite, lpp at STP value of $S^{298°K}_{P = 1\ atm} = 0.534 \times 10^7 ergs/gm°K$

d) Not utilized in calculations.

Table 2

Peak Shock (Impedance Match) States for Gabbroic Anorthosite

Impacting Gabbroic Anorthosite

Impact Velocity (km/sec)	Shock Pressure (Mbar)	Particle Velocity (km/sec)	Shock Velocity (km/sec)	Density (gm/cm^3)	Internal a) Energy Density (10^{10} ergs/gm)
5	0.62[b]	2.50	8.45	4.17	3.13
7.5	0.99[b]	3.75	8.99	5.04	7.03
15.0	3.04[c]	7.50	13.81	6.43	28.13
30.0	10.11[d]	15.0	22.96	8.47	112.50
45.0	21.29[d]	22.50	32.23	9.73	253.13

a) With respect to low-pressure phase of gabbroic anorthosite at STP.

b) Partial melting upon isentropic release.

c) Partial vaporization upon isentropic release.

d) Complete vaporization upon isentropic release.

Table 3

Peak Shock (Impedance Match) States for Iron Impacting Gabbroic Anorthosite

Impact Velocity (km/sec)	Shock Pressure (Mbar)	Particle Velocity[a] Iron (km/sec)	Shock Velocity[a] Iron (km/sec)	Density Iron (gm/cm^3)	Internal Energy Iron (10^{10}ergs/gm)	Particle Velocity Anorthosite (km/sec)	Shock Velocity Anorthosite (km/sec)	Density Anorthosite (gm/cm^3)	Internal Energy Density[b] Anorthosite (10^{10}ergs/gm)
5.0	0.825[c]	1.59	6.60	10.35	1.26	3.41	8.24	5.01	5.81
7.5	1.531[d]	2.51	7.76	11.62	3.15	4.99	10.45	5.62	12.45
15.0	4.807[e]	5.21	11.74	14.13	13.57	9.79	16.72	7.08	47.92
30.0	15.852[f]	10.70	18.85	18.18	57.25	19.30	27.98	9.47	186.25
45.0	33.556[g]	16.35	26.11	21.02	133.66	28.65	39.89	10.42	410.41

a. With respect to iron, at rest.
b. With respect to low-pressure phase of gabbroic anorthosite at STP.
c. Iron solid upon isentropic release; gabbroic anorthosite completely melted upon isentropic release.
d. Iron solid upon isentropic release; gabbroic anorthosite partially vaporized upon isentropic release.
e. Both iron and gabbroic anorthosite partially vaporized upon isentropic release.
f. Gabbroic anorthosite vaporized upon isentropic release; iron partially vaporized.
g. Both iron and gabbroic anorthosite completely vaporized upon isentropic release.

Table 4

Hugoniot Pressures (Mbar) Inducing a Change of State Upon Isentropic Release to Atmospheric Pressure.

	Iron	Gabbroic Anorthosite	
		(ℓpp)	(hpp)
Incipient Melting	2.2	0.97	0.43
Complete Melting	2.6	1.1	0.52
Incipient Vaporization	4.2	1.9	1.02
Complete Vaporization	16.8	7.9	5.9

Table 5

Peak Centerline Pressure Attenuation;

$\log_{10}(P\text{-Mbar}) = a \log_{10}(R/R_o) + b$

	Near-Field			Far-Field		
An → An	a	b	r^2 [(a)]	a	b	r^2 [(a)]
5 km/sec	---	---	---	-1.45	0.151	0.85
15 km/sec	-0.222	0.285	0.83	-1.97	1.399	0.95
45 km/sec	-0.293	1.208	0.92	-2.15	2.373	0.92
Fe → An						
5 km/sec	-0.232	-0.398	0.69	-1.67	0.681	0.91
15 km/sec	-0.295	0.470	0.88	-2.49	1.475	0.97
45 km/sec	-0.149	1.220	0.89	-2.95	2.082	0.99

(a) Linear regression correlation coefficient.

Figure Captions

1. Pressure-particle velocity Hugoniot relation for iron, and low-pressure phase (ℓpp) and high-pressure phase (hpp) assemblage of gabbroic anorthosite. Gabbroic anorthosite Hugoniots are both centered at specific volume of ℓpp and calculated using the Tillotson parameters of Table 1.
2. Hugoniot (H) for iron and calculated critical isentropes, corresponding to incipient melting (IM), complete melting (CM), incipient vaporization (IV) and complete vaporization (CV). The H and IM curves agree closely with similar results obtained by Tillotson (1962).
3. Hugoniot and critical isentropes for ℓpp, gabbroic anorthosite. Curve labeling similar to that in Figure 2.
4. Hugoniot and critical isentropes for hpp, gabbroic anorthosite. Curve labeling similar to that in Figure 2. Compression, V/V_o, corresponds to zero-pressure specific volume of hpp.
5. Log_{10} peak shock pressure, versus, normalized radius at various impact velocities. R_o is radius of impactor for iron object. Parameters of lines fit through calculation are given in Table 5. Arrows (IMS) indicate impedance-match solutions (Table 3) valid for one-dimensional flow.
6. Log_{10} peak shock pressure, versus, normalized radius at various impact velocities for gabbroic anorthosite impactors. Arrows indicate one-dimensional flow pressures (Table 2). Notation is similar to Figure 5.

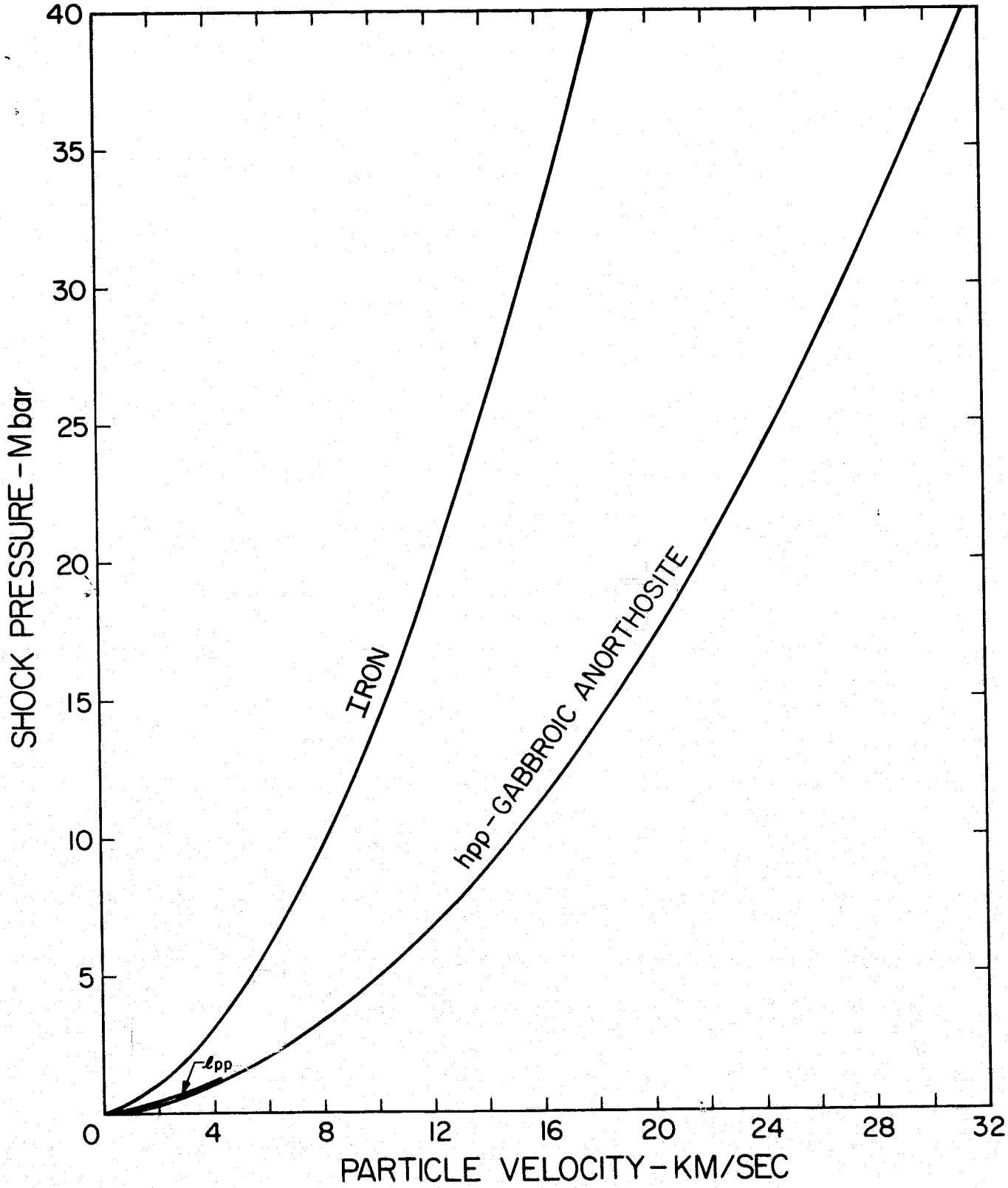
40
35
30
25
20
15
10
5
0
4
8
12
16
20
24
28
32
SHOCK PRESSURE - Mbar
PARTICLE VELOCITY - KM/SEC
IRON
hpp - GABBROIC ANORTHOSITE
ℓpp

Fig. 1

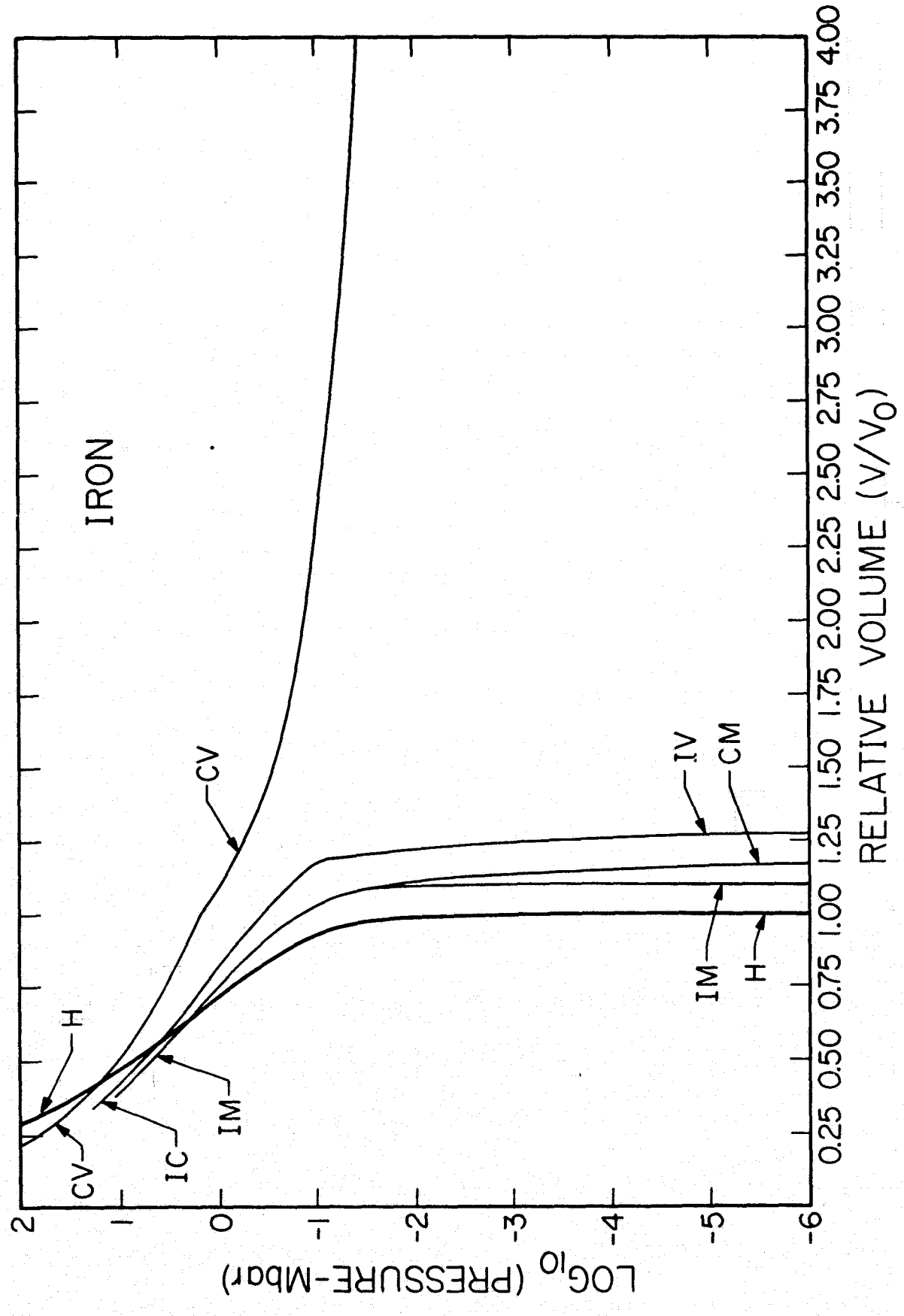

Fig. 2

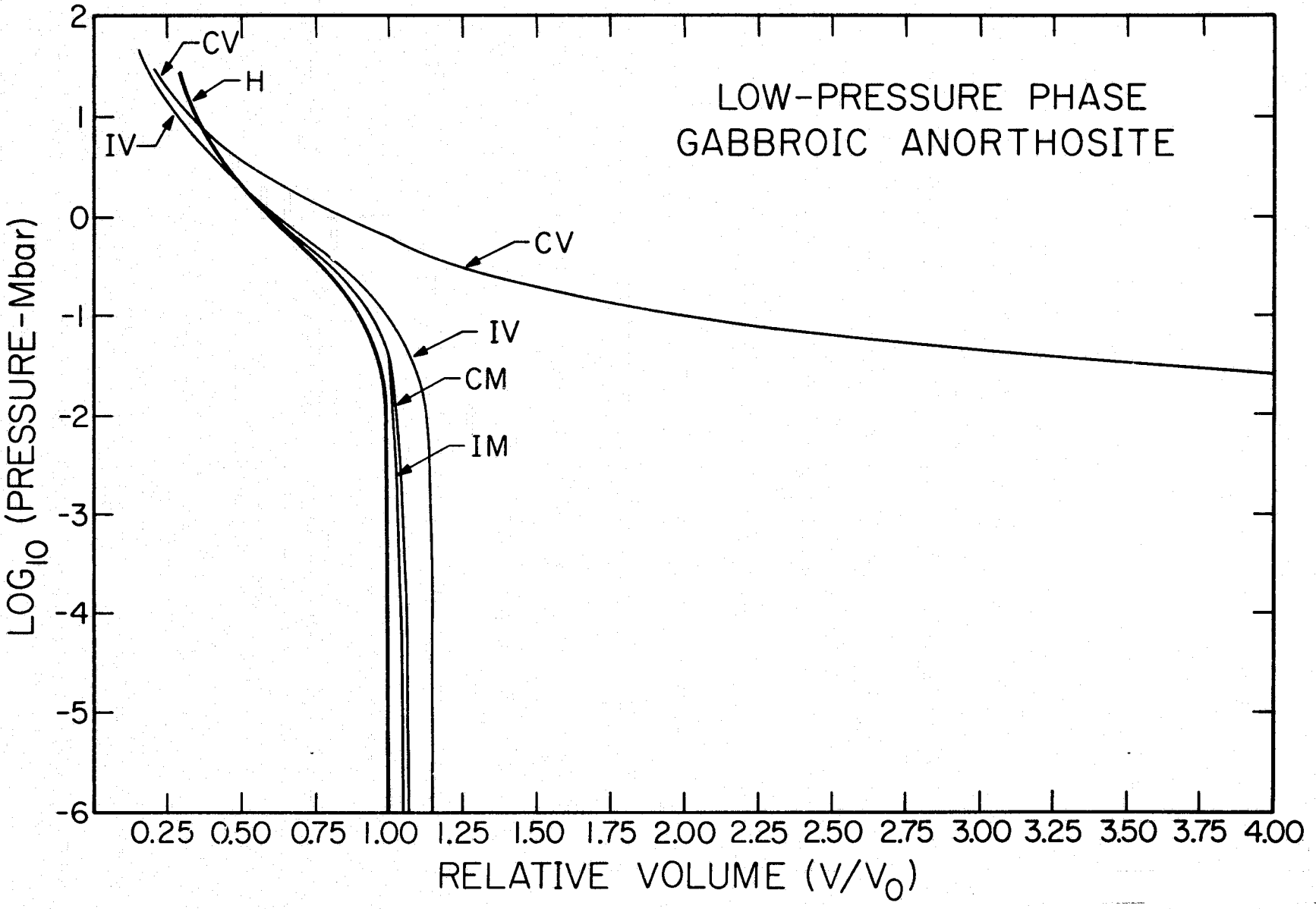
LOW-PRESSURE PHASE
GABBROIC ANORTHOSITE
CV
H
IV
CV
IV
CM
IM
2
1
0
-1
-2
-3
-4
-5
-6
LOG10 (PRESSURE-Mbar)
0.25 0.50 0.75 1.00 1.25 1.50 1.75 2.00 2.25 2.50 2.75 3.00 3.25 3.50 3.75 4.00
RELATIVE VOLUME (V/V0)

Fig. 3

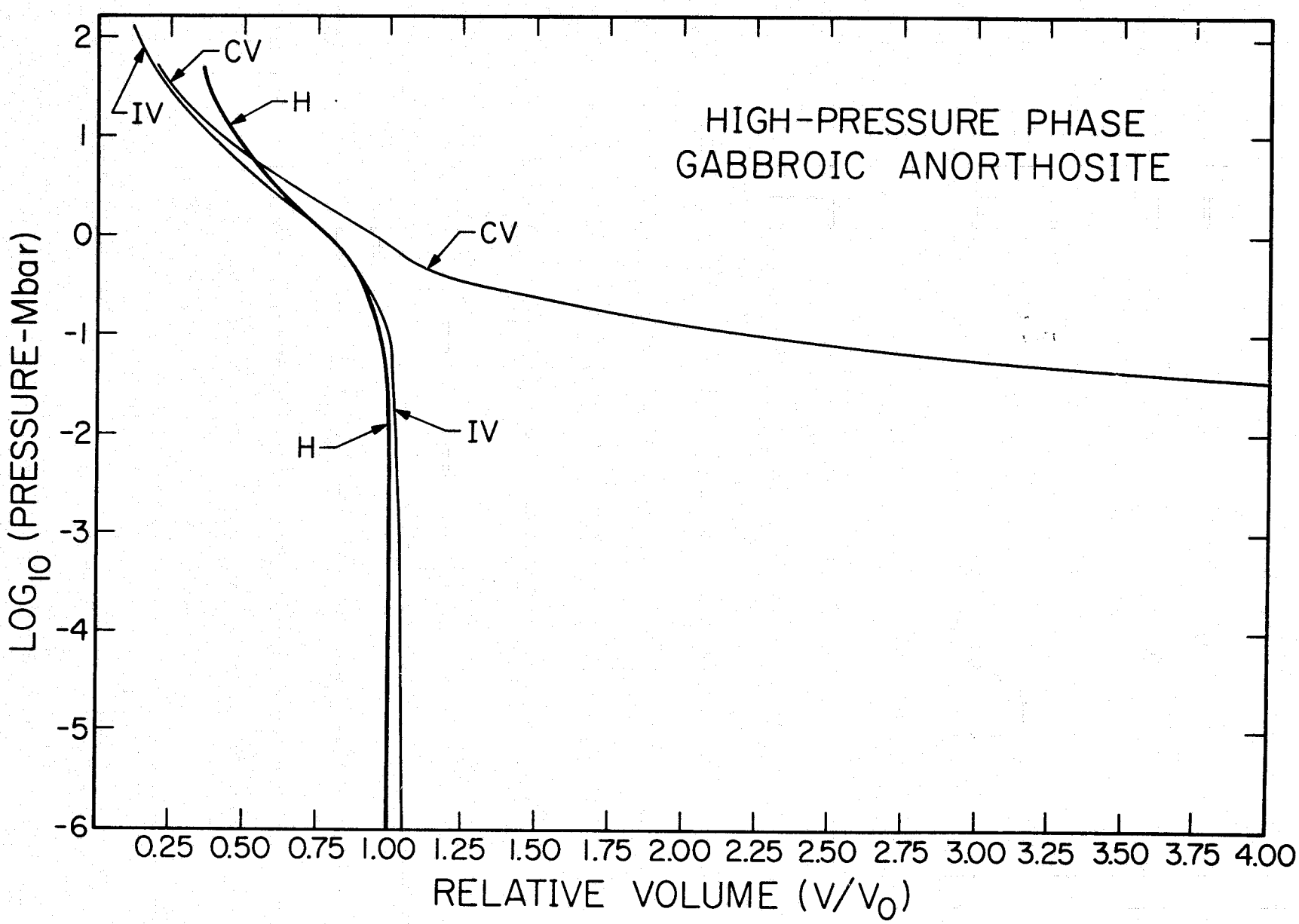
HIGH-PRESSURE PHASE
GABBROIC ANORTHOSITE
CV
IV
H
CV
H
IV
2
1
0
-1
-2
-3
-4
-5
-6
LOG10 (PRESSURE-Mbar)
0.25 0.50 0.75 1.00 1.25 1.50 1.75 2.00 2.25 2.50 2.75 3.00 3.25 3.50 3.75 4.00
RELATIVE VOLUME (V/V0)

Fig. 4

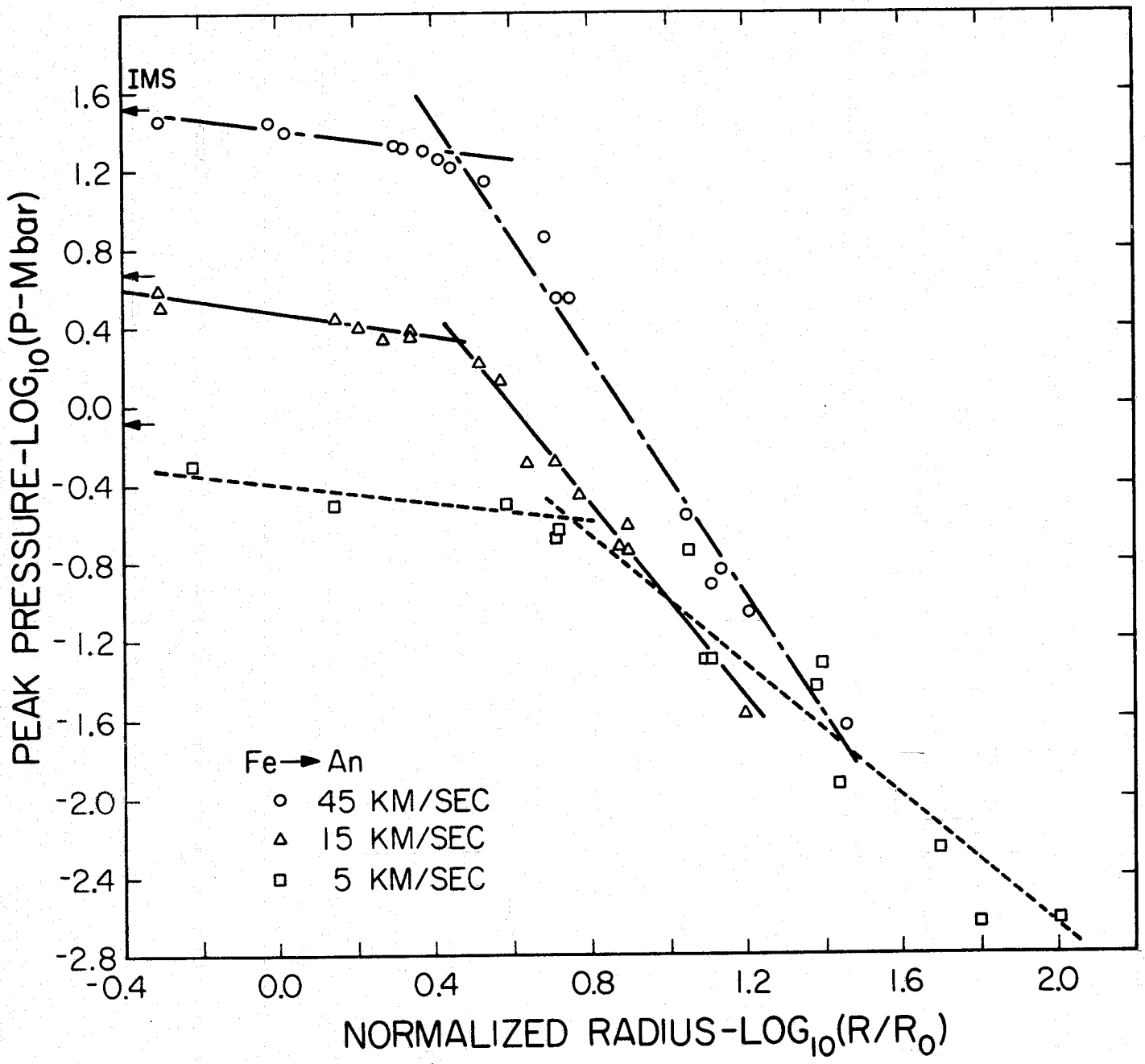
IMS
1.6
1.2
0.8
0.4
0.0
-0.4
-0.8
-1.2
-1.6
-2.0
-2.4
-2.8
-0.4
0.0
0.4
0.8
1.2
1.6
2.0
PEAK PRESSURE-LOG10(P-Mbar)
NORMALIZED RADIUS-LOG10(R/R0)
Fe→An
45 KM/SEC
15 KM/SEC
5 KM/SEC

Fig. 5

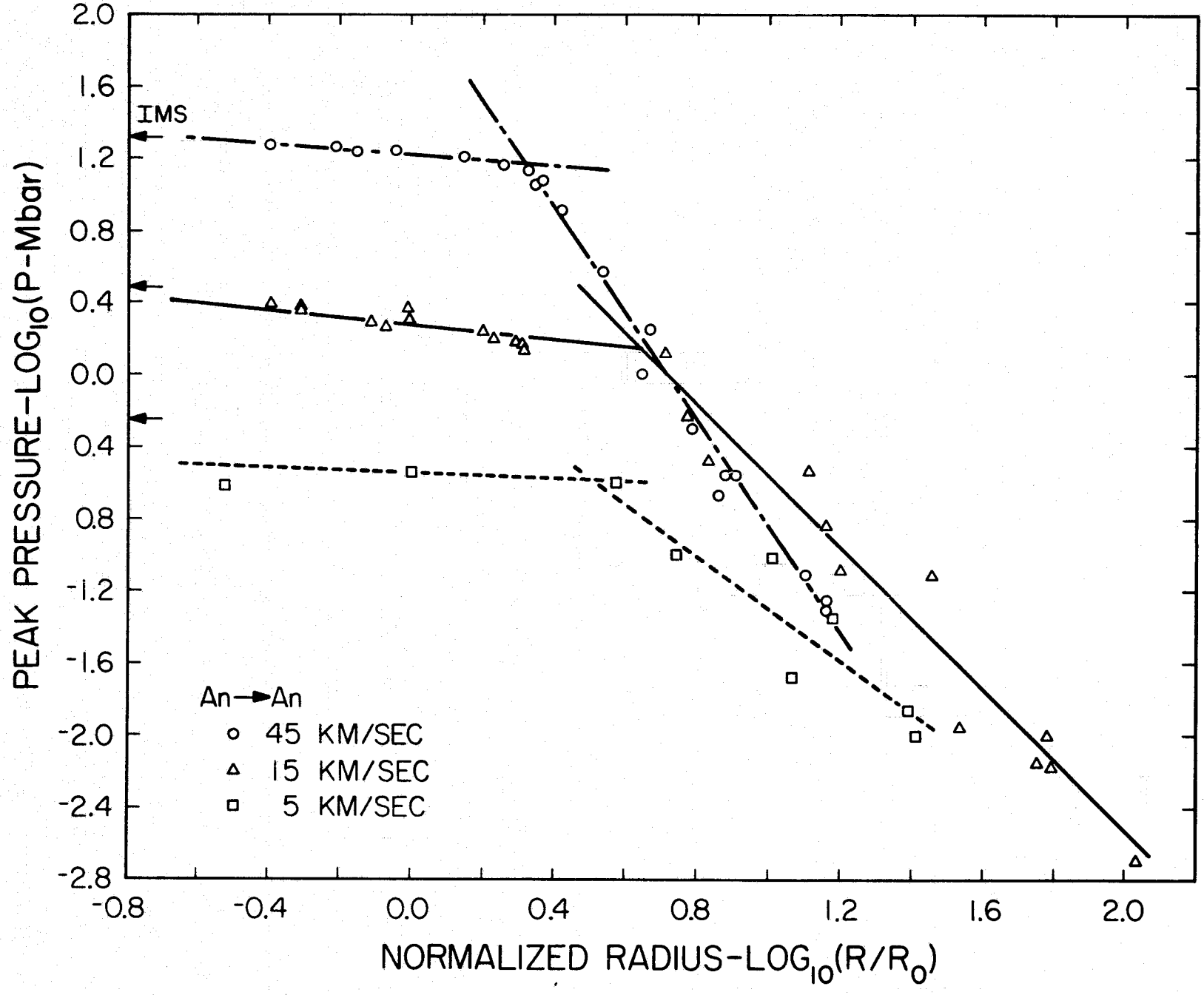
2.0
1.6
1.2
0.8
0.4
0.0
0.4
0.8
-1.2
-1.6
-2.0
-2.4
-2.8
IMS
PEAK PRESSURE-LOG10(P-Mbar)
An→An
45 KM/SEC
15 KM/SEC
5 KM/SEC
-0.8
-0.4
0.0
0.4
0.8
1.2
1.6
2.0
NORMALIZED RADIUS-LOG10(R/R0)

Fig. 6